01 Jan 2003

Impedance Boundary Conditions in a Hybrid FEM/MOM Formulation

Hao Wang

Minjia Xu

Chen Wang

Todd H. Hubing
Missouri University of Science and Technology

Recommended Citation

H. Wang et al., "Impedance Boundary Conditions in a Hybrid FEM/MOM Formulation," *IEEE Transactions on Electromagnetic Compatibility*, Institute of Electrical and Electronics Engineers (IEEE), Jan 2003.
The definitive version is available at https://doi.org/10.1109/TEMC.2003.810813

Impedance Boundary Conditions in a Hybrid FEM/MOM Formulation

Hao Wang, Minjia Xu, *Member, IEEE*, Chen Wang, *Student Member, IEEE*, and Todd Hubing, *Senior Member, IEEE*

***Abstract*—When numerically modeling structures with imperfect conductors or conductors coated with a dielectric material, impedance boundary conditions (IBCs) can substantially reduce the amount of computation required. This paper incorporates the IBC in the finite-element method (FEM) part of a FEM/method of moments (FEM/MoM) modeling code. Properties of the new formulation are investigated and the formulation is used to model three practical electromagnetic problems. Results are compared to either measured data or other numerical results. The effect of the IBC on the condition number of hybrid FEM/MoM matrices is also discussed.**

***Index Terms*—Electromagnetic (EM) modeling, finite element method (FEM), method of moments (MoM).**

I. Introduction

TO SOLVE Maxwell's equations, the specification of the boundary conditions at the interface of different materials is required. In many cases, simpler approximate boundary conditions that account for the presence of an imperfect thin conducting structure, a thin dielectric sheet, or an inhomogeneous medium are employed to simulate the actual surface and thereby avoid excessive computation. The pioneering investigations of Leontovich [1] showed that the observed phenomenon in these cases could be represented by imposing an impedance boundary condition (IBC) to represent the actual surface. A detailed study of the IBC was made by Senior [2], in which the fundamental assumptions inherent in the IBC were examined by considering a plane wave impinging upon a material half space.

There are two primary formulations for IBCs in the frequency domain. The first formulation is based on the integral-equation method of moments (MoM). Mitzner [4] presented a magnetic-field integral equation (MFIE) for bodies satisfying the IBC. Heath [5] and Medgyesi–Mitschang [6] examined a combined-field integral equation (CFIE) that was immune to the interior resonance problem. The other primary formulation is based on the finite-element method (FEM). Jin [7] and Volakis [3] incorporated an impedance boundary in FEM volumes. This paper investigates this IBC incorporated in the FEM part of a hybrid FEM/MoM code.

When analyzing electromagnetic compatibility (EMC) problems, two kinds of structures are frequently encountered that are readily modeled using impedance boundaries. One such structure is a very thin dielectric sheet with a permittivity much higher than that of surrounding materials. For this case, it is difficult to enforce the exact boundary conditions imposed at the interface due to the excessive computational cost and unstable results. By simulating the dielectric sheet with a zero-thickness resistive sheet and using IBC, this kind of structure can be modeled efficiently. Another structure readily modeled using IBCs is a thin, lossy conductor with a thickness greater than the skin depth. At high frequencies, the loss due to imperfect conductors can have a significant effect and therefore cannot be neglected.

Full-wave hybrid FEM/MoM methods are well suited for analyzing geometries that include both small inhomogeneous structures and larger radiating conductors. They have been successfully used to solve scattering problems [8] and to analyze printed circuit board geometries [9].

This paper incorporates the IBC proposed in [3] and [7] in the FEM part of a FEM/MoM modeling code. Properties of the new formulation are investigated and the formulation is used to model practical electromagnetic problems. Results are obtained for three electromagnetic problems. The first problem is the scattered field from a thin, dielectric, spherical shell. This is one of the canonical problems proposed by the Germany Chapter of the IEEE EMC Society. The second problem is the analysis of a printed circuit board power bus structure whose top and bottom planes are not perfect electric conductors (PEC). In this case, the loss of the imperfect conductors must be considered to obtain accurate results. The third geometry analyzed is an asymmetric stripline structure. Results are compared to either measured data or other numerical results.

II. Formulation

As shown in Fig. 1, the IBC implies that the electric field $\mathbf{E}$ above the impedance boundary S_k and the total magnetic fields $\mathbf{H}^{\pm}$ above and below the boundary can be related to one another by the material properties (i.e., surface impedance) or the surface characteristics such as roughness. The fields are assumed to satisfy the boundary condition [7]

$$\hat{\mathbf{n}}_k \times (\hat{\mathbf{n}}_k \times \mathbf{E}) = -\eta_S \eta_0 \hat{\mathbf{n}}_k \times (\mathbf{H}^+ - \mathbf{H}^-) \tag{1}$$

where $\hat{\mathbf{n}}_k$ is the unit normal vector that points from the impedance surface S_k into the computational domain (+ side), $\eta_0 = \sqrt{\mu_0/\varepsilon_0} = 377\ \Omega$; η_S is the relative surface impedance.

Manuscript received July 15, 2002; revised December 15, 2002.

H. Wang was with the University of Missouri-Rolla, Rolla, MO 65409 USA (e-mail:hubing@umr.edu). He is now with Micron Technology Inc., Boise, ID USA.

M. Xu is with Hewlett-Packard Company, San Diego, CA 92127 USA.

C. Wang and T. Hubing are with the University of Missouri-Rolla, Rolla, MO 65409 USA (e-mail:hubing@umr.edu).

Digital Object Identifier 10.1109/TEMC.2003.810813

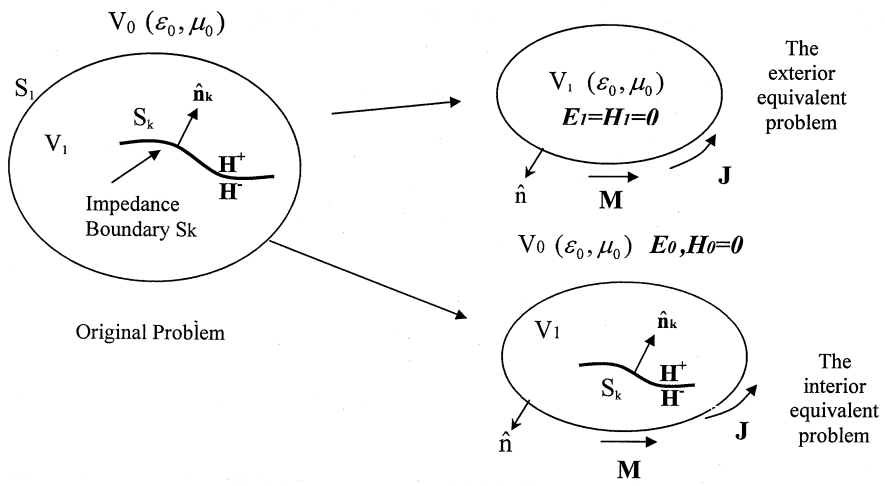

Fig. 1. FEM/MoM with impedance boundary formulation.

When the surface is totally impenetrable, (1) can be simplified as

$$\hat{\mathbf{n}}_k \times (\hat{\mathbf{n}}_k \times \mathbf{E}) = -\eta_S \eta_0 \hat{\mathbf{n}}_k \times \mathbf{H}. \tag{2}$$

According to the equivalence theorem [8], the original problem in Fig. 1 can be decomposed into two parts: the exterior equivalent problem and the interior equivalent problem. To solve for the fields ($\mathbf{E}_0$, $\mathbf{H}_0$) in V_0, equivalent electric currents $\mathbf{J}$ and equivalent magnetic currents $\mathbf{M}$ are introduced to positions just above the fictitious boundary between V_0 and V_1. All fields in V_1 are set to zero. Now, the exterior equivalent problem is a homogeneous problem. The homogeneous Green's function can be used as the kernel to formulate an integral equation and the MoM can be used to solve it. Similarly, for the interior equivalent problem, the fields in V_0 are set to zero while the surface currents $\mathbf{J}$ and $\mathbf{M}$ are introduced on the boundary to solve for the fields ($\mathbf{E}_1$, $\mathbf{H}_1$) in V_1. The FEM is employed to analyze the interior equivalent problem. The two equivalent problems are related by forcing the continuity of the tangential fields at the interface between FEM and MoM. In this paper, the impedance boundary S_k is handled in the FEM part.

Considering the impedance boundary S_k, the following weak form of the $\mathbf{E}$ field is obtained in the FEM part [9]:

$$\begin{aligned}\int_{V_1} \left[\left(\frac{\nabla \times \mathbf{E}(r)}{j\omega\mu_0\mu_r} \right) \cdot (\nabla \times \mathbf{w}(r)) + j\omega\varepsilon_0\varepsilon_r \mathbf{E}(r) \cdot \mathbf{w}(r) \right] dV \\ = -\int_{S_k} \frac{1}{\eta_S \eta_0} (\hat{\mathbf{n}}_k \times \mathbf{E}(r)) \cdot (\hat{\mathbf{n}}_k \times \mathbf{w}(r))\, dS \\ + \int_{S_1} (\hat{n} \times \mathbf{H}(r)) \cdot \mathbf{w}(r)\, dS - \int_{V_1} \mathbf{J}^{int}(r) \cdot \mathbf{w}(r)\, dV\end{aligned} \tag{3}$$

where S_1 is the surface enclosing volume V_1, and $\mathbf{w}(r)$ is a weighting function. In this study, vector tetrahedral edge elements [11] were used as basis functions and weighting functions.

The electric field $\mathbf{E}$ within the volume V_1 can be expanded as

$$\mathbf{E}(\mathbf{r}) = \sum_{n=1}^{N_V} E_n \mathbf{w}_n(\mathbf{r}) \tag{4}$$

where N_v is the total number of interior edges in V_1, dielectric boundary edges on S_1 and impedance boundary edges on S_k. Equation (3) can be discretized as

$$\begin{bmatrix} A_{ii} & A_{ik} & A_{id} \\ A_{ki} & A_{kk} - S_{kk} & A_{kd} \\ A_{di} & A_{dk} & A_{dd} \end{bmatrix} \begin{bmatrix} E_i \\ E_k \\ E_d \end{bmatrix} = \begin{bmatrix} 0 & 0 & 0 \\ 0 & 0 & 0 \\ 0 & 0 & B_{dh} \end{bmatrix} \begin{bmatrix} 0 \\ 0 \\ J_h \end{bmatrix} + [g^{int}] \tag{5}$$

where the unknown coefficients $[E_n]$ are partitioned according to edge type. The three categories are interior edges, which are denoted by the subscript i, dielectric boundary edges, which are denoted by the subscript d, and impedance boundary edges, which are denoted by the subscript k. $[J_h]$ describes currents on dielectric boundary edges and edges that are on both conductor and dielectric boundaries. The elements of $[A]$, $[B_{dh}]$, $[S_{kk}]$ and $[g^{int}]$ are given by

$$A_{mn} = \int_{V_1} \left[\frac{(\nabla \times w_n(\mathbf{r})) \cdot (\nabla \times w_m(\mathbf{r}))}{j\omega\mu_0\mu_r} + j\omega\varepsilon_o\varepsilon_r w_n(\mathbf{r}) \cdot w_m(\mathbf{r}) \right] dV \tag{6}$$

$$S_{mn} = \int_{S_k} -\frac{1}{\eta_S \eta_0} (\hat{n}_k \times w_m(\mathbf{r})) \cdot (\hat{n}_k \times w_n(\mathbf{r}))\, dS \tag{7}$$

$$B_{mn} = \int_{S_d} \mathbf{f}_n(\mathbf{r}) \cdot w_m(\mathbf{r})\, dS \tag{8}$$

$$g_m^{int} = -\int_{V_1} \mathbf{J}^{int} \cdot w_m(\mathbf{r})\, dV \tag{9}$$

where $\mathbf{f}_n(\mathbf{r})$ are surface basis functions. In this study, *Rao–Wilton–Glisson* triangular surface basis functions were employed [12]. Since the tangential $\mathbf{E}$ field vanishes on the PEC part of S_1, B_{mn} is evaluated over the dielectric part, S_d, rather than all of S_1. S_{mn} is the term associated with IBC and is evaluated over the impedance boundary edges.

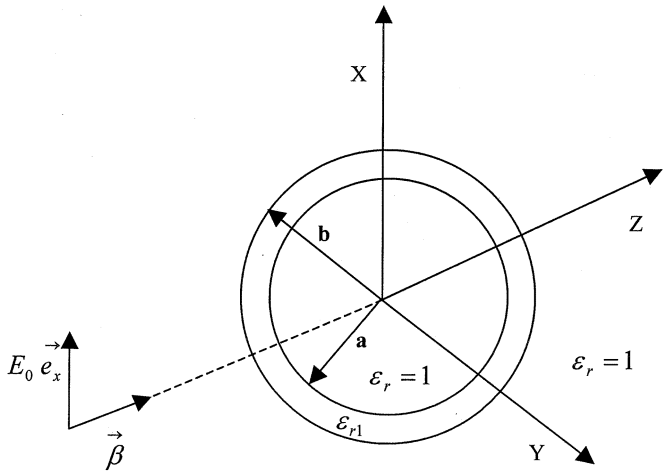

Fig. 2. Scattering of a plane wave by a hollow coated sphere.

For the exterior equivalent problem, the electric-field integral equation (EFIE) [13] is used

$$\mathbf{E}^{\text{inc}}(\mathbf{r}) = \tfrac{1}{2}\,\mathbf{E}(\mathbf{r}) + \int_{S_1} \Big\{ \mathbf{M}(\mathbf{r}') \times \nabla' G_0(\mathbf{r}, \mathbf{r}') + jk_0\eta_0 \mathbf{J}(\mathbf{r}') G_0(\mathbf{r}, \mathbf{r}') - j\,\frac{\eta_0}{k_0}\,\nabla' \cdot \mathbf{J}(\mathbf{r}') \nabla' G_0(\mathbf{r}, \mathbf{r}') \Big\}\, dS' \qquad (10)$$

where k_0 is the wavenumber in free space. $G_0(\mathbf{r}, \mathbf{r}')$ is the Green's function in free space.

The equivalent surface electric and magnetic currents are defined as

$$\mathbf{J}(\mathbf{r}) = \hat{\mathbf{n}} \times \mathbf{H}(\mathbf{r}), \qquad \mathbf{r} \in S_1 \qquad (11)$$

$$\mathbf{M}(\mathbf{r}) = \mathbf{E}(\mathbf{r}) \times \hat{\mathbf{n}}, \qquad \mathbf{r} \in S_d. \qquad (12)$$

Equations (3) and (10) can be solved by *outward-looking*, *inward-looking*, or *combined methods* [14].

III. Numerical Results

The IBC formulation described above was incorporated in the Electromagnetic Analysis Program Version 5 (EMAP5) hybrid FEM/MoM modeling code [15]. Three example geometries that are more efficiently modeled using IBCs are investigated below. Results obtained from the FEM/MoM formulation are compared to results obtained using other well-established codes, measurements, or analytical results.

A. The Scattered Field From a Spherical Shell

The first example considered here is the scattered field from a thin, dielectric, spherical shell. This problem was proposed by the Germany Chapter of the IEEE EMC Society and is described on their web page at **http://www-tet.uni-paderborn.de**. As shown in Fig. 2, a hollow sphere with inner and outer radii a and b, $b/a = 1.001$ and $a = 9$ cm, is centered at the origin of the coordinate system. The shell is made up of a dielectric material with relative permittivity $\varepsilon_{r1} = 1000$. The hollow sphere is located in free space.

Since the shell is thin geometrically as well as electrically and $\varepsilon_{shell} \gg 1$, the IBC (1) previously used in [16] can again be applied here. In this case, the thin dielectric shell is replaced by a boundary without thickness. The boundary conditions for the tangential components of the fields on the thin shell are given in (1), where

$$\eta_S \eta_0 = \frac{j}{\omega(\varepsilon_{r1} - \varepsilon_0)\, d} \qquad (13)$$

is the resistance of the shell, d being the thickness of the shell.

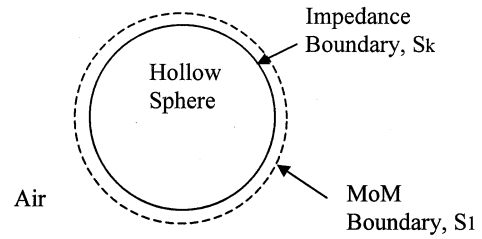

Fig. 3. FEM boundary and MoM boundary.

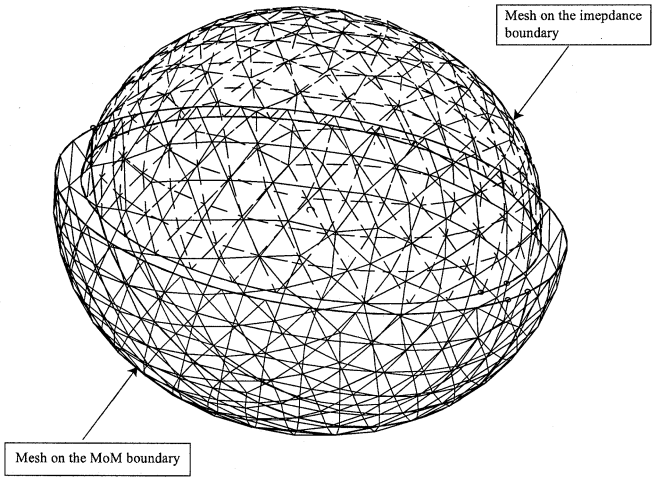

Fig. 4. Triangular meshes on the impedance and MoM boundaries.

To solve this problem, the meshing strategy shown in Fig. 3 is used. The dashed circle is the fictitious MoM boundary, S_1, located in free space. The hollow sphere with the impedance boundary, S_k, and an air gap are included in the FEM part. One of the advantages of this strategy is that S_k can be discretized into more elements without increasing computational time and memory significantly since FEM elements require fewer computer resources than MoM elements. Fig. 4 illustrates the triangular mesh on the impedance boundary S_k and the MoM boundary S_1. Fig. 5 shows the bistatic scattering cross section at 583 MHz obtained using FEM/MoM with an impedance boundary and Mie series. The Mie Series formulation models spheres like this without much difficulty and the Mie series result can be considered accurate. The difference between these two results is within 1 dB.

B. The Input Impedance of a Power Return Plane Structure

The second problem geometry is a rectangular printed circuit board power-return plane pair separated by a dielectric substrate as shown in Fig. 6. The board modeled in this study is 1.52 by 1.02 cm with two imperfectly conducting planes. These two planes are separated by an 8-mil layer of embedded capacitance

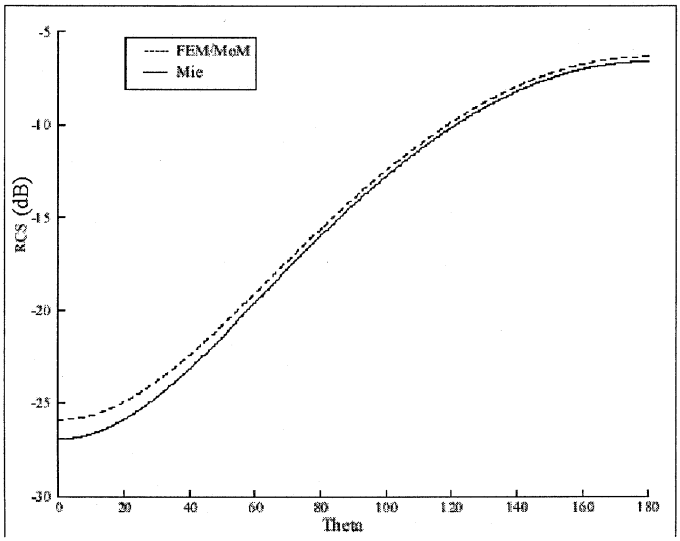

Fig. 5. Bistatic scattering cross section of a hollow sphere.

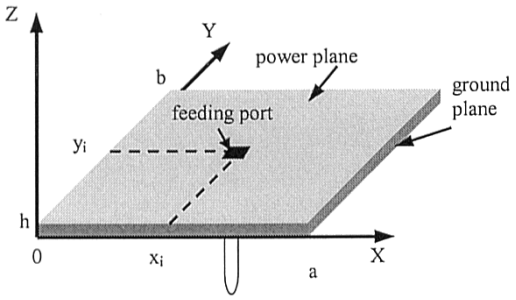

Fig. 6. Geometry of a rectangular power-return plane structure.

material [17] with a relative permittivity equal to 21.5 and a loss tangent equal to 0.04. The conductivity of the planes is 7.0×10^4 S/m.

A coaxial cable feeds the board at the location (0.56 cm, 0.52 cm). The equivalent radius concept is employed to model the coaxial-cable feed by replacing the circular cross section of the center conductor of the coaxial cable with a rectangular strip with an "equivalent" radius [18]. To model the coaxial-cable feed, two current sources located at the two sides of the rectangular strip are connected in parallel then the total current following from the center conductor to the outer conductor is $2I_1$ [24].

Power-return plane pairs in unpopulated printed circuit boards exhibit four kinds of losses. There is loss due to the finite conductivity of the power and ground planes, loss in the dielectric, radiation loss, and losses due to surface waves induced on the outer surface of the power and ground planes. At frequencies below 10 GHz, the surface wave loss can be neglected [19]. The finite conductivity loss can be modeled by an IBC; the dielectric loss is represented by the imaginary part of the dielectric permittivity, which is included in the FEM formulation; and the radiation loss can be calculated from the equivalent surface electric and magnetic currents on the MoM boundary.

The presence of the imperfect conductor planes creates a finite tangential electric field, E_T, corresponding to the current

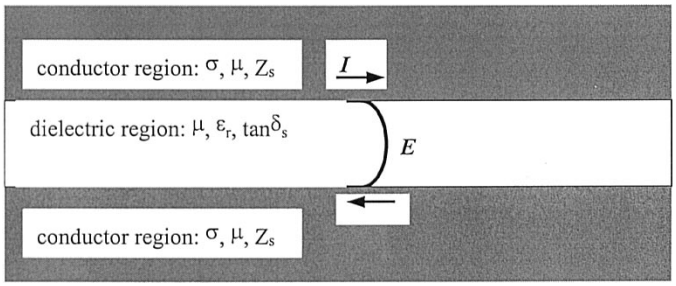

Fig. 7. Field inside a dielectric substrate between imperfect conductors.

flowing along the conductor. Consequently, the overall electric field at the boundary between the conductor and the dielectric substrate may no longer be perpendicular to the conducting planes as illustrated in Fig. 7. In order to model this variation of the tangential electric field in the vertical direction, the dielectric substrate is divided into three layers and meshed into 20 600 tetrahedra. The power and the return planes are discretized into 3732 triangular patches.

To model the effects of the finite conductivity of the power and ground planes, Equation (1) is used, which also can be expressed as

$$E_t = Z_S J_S \tag{14}$$

where

$$Z_S = (1+j)R_S = (1+j)(1/\sigma\delta) = (1+j)\sqrt{\pi f \mu_0/\sigma}. \tag{15}$$

There are three assumptions in this expression.

- Both the power and ground planes are much thicker than the skin depth of the conductor.
- J_S is the superposition of the electric currents flowing on the top and bottom surfaces of the conductor.
- The total tangential electric field above the inner surface of the conductor is identical to the tangential electric field below the inner surface of the conductor.

To validate the EMAP5 result, a resonant cavity model was also used to calculate the input impedance of this structure. The cavity model is widely employed to characterize printed circuit board power-return plane structures [20]–[22]. The input and transfer impedance of the power-return plane pair is obtained using a mode-expansion method

$$\begin{aligned} Z_{ij} = j\omega\mu h \sum_{m=0}^{\infty}\sum_{n=0}^{\infty} \frac{\chi_{mn}^2}{ab(k_{xm}^2 + k_{yn}^2 - k^2)} \\ \times \cos(k_{yn}y_i)\cos(k_{xm}x_i)\operatorname{sinc}\left(\frac{k_{yn}\,dy_i}{2}\right)\operatorname{sinc}\left(\frac{k_{xm}\,dx_i}{2}\right) \\ \times \cos(k_{yn}y_j)\cos(k_{xm}x_j)\operatorname{sinc}\left(\frac{k_{yn}\,dy_j}{2}\right)\operatorname{sinc}\left(\frac{k_{xm}\,dx_j}{2}\right). \end{aligned} \tag{16}$$

A detailed explanation and applications of (16) can be found in [22]. Fig. 8 compares the FEM/MoM result with the cavity model result. Despite the highly different approaches that these two methods take, the results are in close agreement. Fig. 9

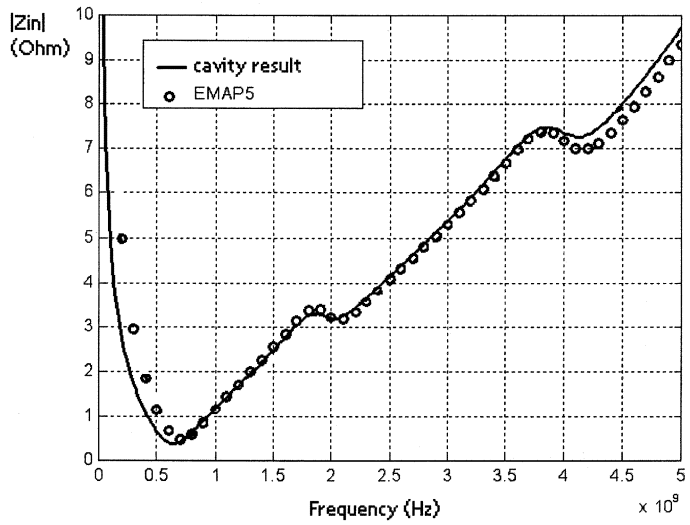

Fig. 8. Input impedance of an 8-mil 1.52-cm by 1.02-cm board made from graphite and embedded capacitance material.

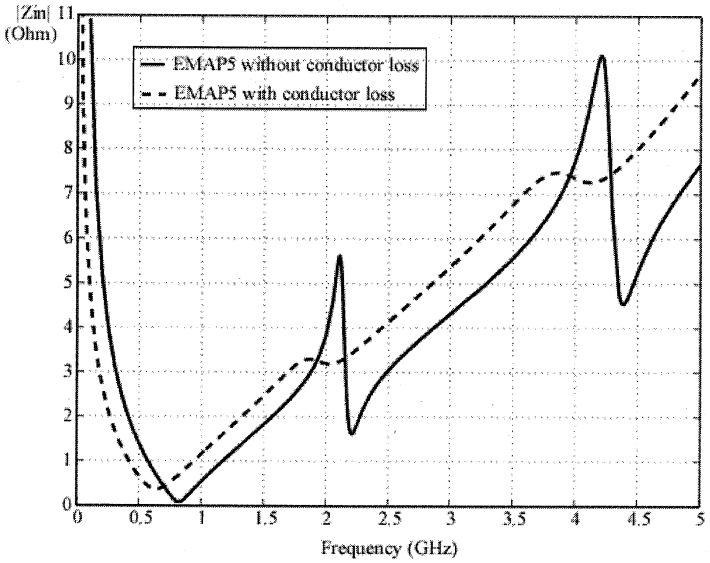

Fig. 9. Input impedance comparison with and without conductive loss.

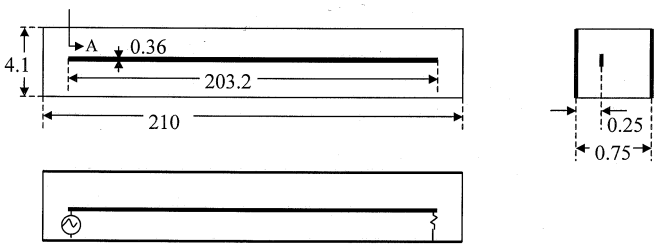

Fig. 10. Geometry of the stripline board (units are in millimeters).

compares the calculated input impedance with and without conductor loss. It can be seen that the losses in the conductors play a significant role and cannot be neglected.

C. Lossy Stripline Structure

The third problem geometry is a stripline structure on a 210-mm × 4.1-mm × 0.75-mm printed circuit board. The top and bottom layers of the board are metal planes, whereas the inner layer located at 1/3 of the thickness of the board has a 203.2-mm-long and 0.36-mm-wide trace. The geometry of the stripline structure and the dielectric constant and loss tangent of the board are shown in Figs. 10 and 11, respectively. The system is driven at Port 1 by a current source and terminated at Port 2 by a 50-Ω load.

A commercial mesh generator is used to mesh the stripline structure. As shown in Fig. 12, in order to get an accurate result, the width of the trace is discretized into four cells and the thickness of the board is discretized into six cells. Because the cell size is very small, the FEM volume is divided into 35 643 tetrahedra. The power and the return planes are discretized into 6983 triangular patches. Two simulations are performed, one with the metal modeled as a PEC, and the other with the metal modeled with the conductivity of copper ($\sigma = 5.7 \times 10^7$ S/m). Equation (15) is used to represent the copper loss. In (5), $[J_h]$ represents the equivalent current density on the dielectric boundary. From

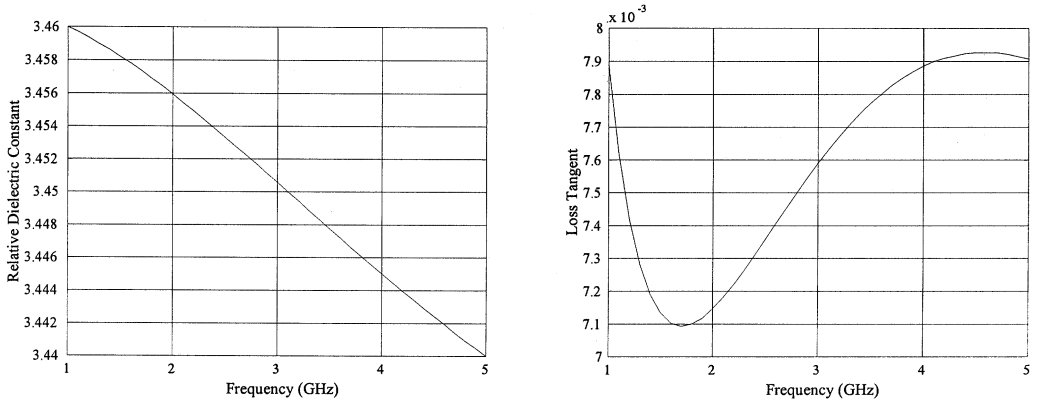

Fig. 11. Properties of the stripline dielectric.

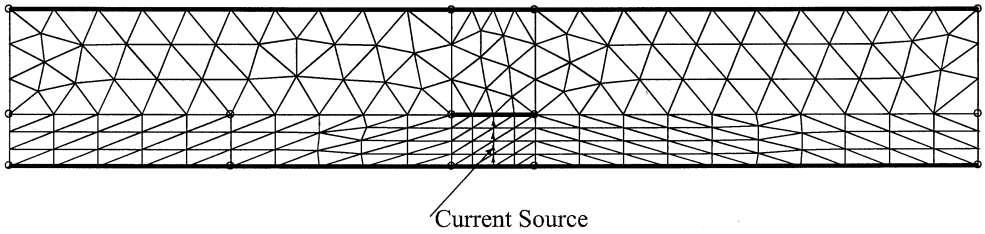

Fig. 12. Cross section of the FEM mesh.

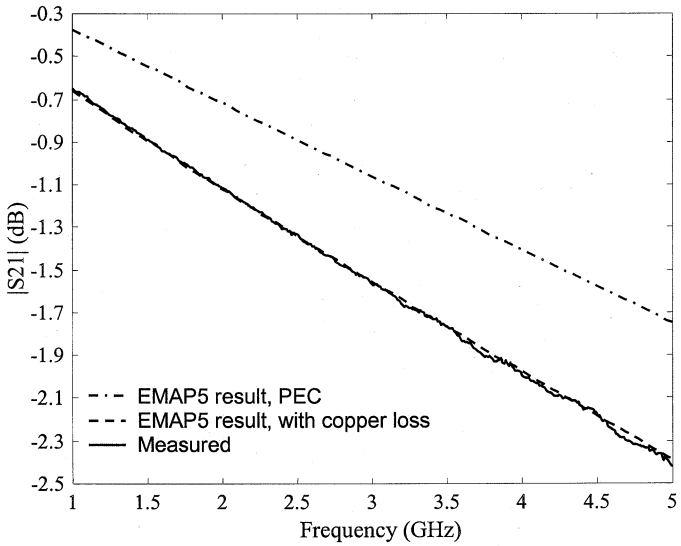

Fig. 13. Measured and modeled S_{21} results.

[23], $[J_h]$ can be set to zero to indicate negligible radiation loss. Then, (5) can be rewritten as

$$\begin{bmatrix} A_{ii} & A_{ik} & A_{id} \\ A_{ki} & A_{kk} - S_{kk} & A_{kd} \\ A_{di} & A_{dk} & A_{dd} \end{bmatrix} \begin{bmatrix} E_i \\ E_k \\ E_d \end{bmatrix} = \left[g^{int}\right]. \tag{17}$$

Equation (17) is a pure FEM equation that can be solved independently. The advantage of this simplification is that the volume can be discretized into more elements and take full advantage of the sparsity of the FEM matrix. Fig. 13 illustrates the measured and modeled S_{21} results. The curve corresponding to the modeled results without copper loss, is approximately 0.4–0.9 dB higher than the measured result. The dashed curve, corresponding to the EMAP5 modeling with copper loss, is very close to the measurement results.

IV. Matrix Condition Number

IBCs can substantially reduce the number of elements required to solve many problems. However, they can also affect the condition of the FEM matrix, which can adversely affect solution times. Iterative solvers are widely used to solve large sparse matrix equations. The convergence rate of iterative solvers depends on the condition number of the matrix M, which is defined as [14]

$$K(M) = \sqrt{\frac{\lambda_{\max}}{\lambda_{\min}}} \tag{18}$$

where $\lambda_{\min}$ and $\lambda_{\max}$ are the smallest and largest eigenvalues of the matrix $M^H M$, where M^H is the transpose conjugate of M. A matrix with a large condition number is nearly singular or *ill-conditioned*. An ill-conditioned linear system is very sensitive to small changes in the matrix. Iterative solvers may not converge smoothly, or may even diverge when applied to ill-conditioned systems.

Incorporating IBC in a FEM matrix will bring about the transformation below for the FEM matrix

$$\begin{bmatrix} A_{ii} & A_{ik} & A_{id} \\ A_{ki} & A_{kk} & A_{kd} \\ A_{di} & A_{dk} & A_{dd} \end{bmatrix} \Rightarrow \begin{bmatrix} A_{ii} & A_{ik} & A_{id} \\ A_{ki} & A_{kk} - S_{kk} & A_{kd} \\ A_{di} & A_{dk} & A_{dd} \end{bmatrix} \tag{19}$$

where the magnitude of the elements of S_{kk} is inversely proportional to the magnitude of the surface impedance η, where $\eta = \eta_S \eta_0$. When the magnitude of η is large (high-impedance

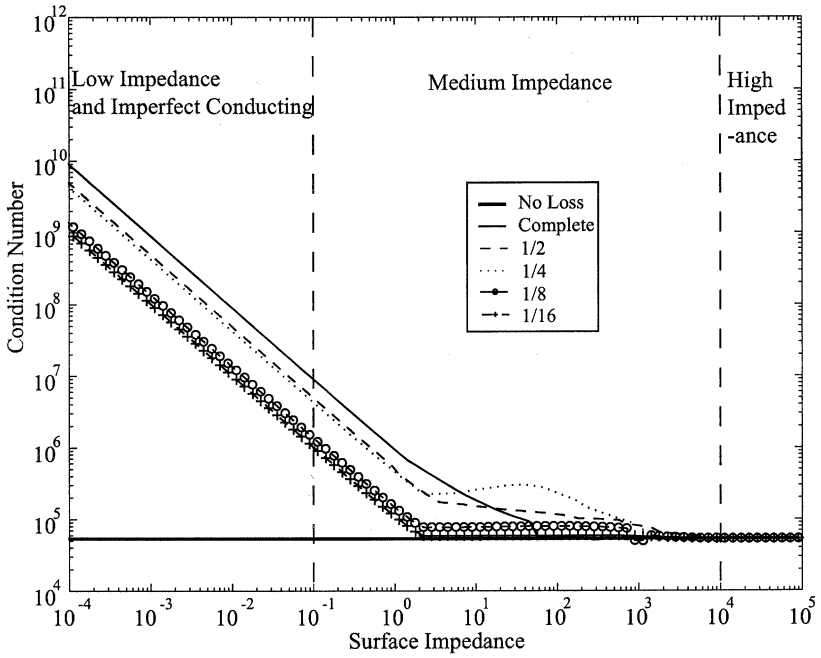

Fig. 14. Condition numbers at frequency 583 MHz.

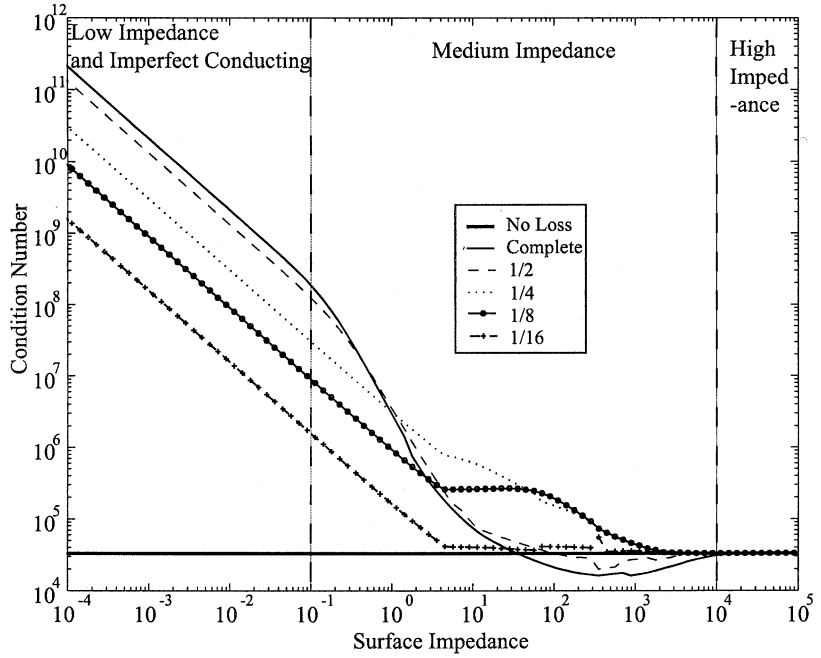

Fig. 15. Condition numbers at frequency 1066 MHz.

boundary), S_{kk} is very small; when the magnitude of η is small (low-impedance boundary or imperfect conducting boundary), S_{kk} is large. In the limit, as $\eta_S \rightarrow 0$, the matrix becomes singular.

For the lossy sphere problem described earlier, Figs. 14 and 15 illustrate the condition numbers of the final hybrid FEM/MoM matrices corresponding to different magnitudes of η at 583 MHz and 1066 MHz respectively. For a sphere without the impedance boundary, the result is denoted as "No Loss;" for a sphere fully covered by the impedance boundary, the result is denoted as "Complete;" for a sphere half covered by the impedance boundary, the result is denoted as "1/2." Similarly, "1/4," "1/8," and "1/16" denote the results corresponding to different numbers of impedance boundary edges. Compared with the "Complete" results, the x axis is divided into three areas from left to right.

- Low-loss impedance boundary and imperfect conducting boundary ($|\eta| < 10^{-1}$): The condition numbers of the FEM/MoM matrices decrease at the rate of -10 dB/decade.

- Medium-loss impedance boundary ($10^{-1} < |\eta| < 10^{4}$): The condition numbers of the FEM/MoM matrices vary.
- High-loss impedance boundary ($|\eta| > 10^{4}$): The condition numbers of the FEM/MoM matrices remain fixed at the "complete" result.

Although the condition of the FEM matrix depends on many factors, it is apparent from this example that IBCs for low-impedance boundaries can significantly affect the stability of the matrix solution. IBCs with lower impedances have a greater effect. Therefore, when modeling a good conductor such as copper ($|\eta|$ is in the order of 10^{-3} from 100 MHz to 1 GHz), the condition numbers of the hybrid FEM/MoM matrices will be much larger than they would be if the copper had been modeled as PEC and IBCs not used.

V. Conclusion

The hybrid FEM/MoM formulation including the IBC was presented in this paper. Incorporating IBC in the hybrid FEM/MoM allows users to analyze geometries with thin dielectric sheets or imperfect conductors more efficiently. Three practical problems were modeled to validate the formulation and to demonstrate methods for applying the IBC to different geometries. Good agreement was achieved between the FEM/MoM formulation and other well-established codes, analytical results, or measurements. The effects of the IBC terms on the condition numbers of the final FEM/MoM matrices were also discussed.

References

[1] M. A. Leontovich, *Investigation of Propagation of Radiowaves*. Moscow, U.S.S.R.: Acad. Sci., 1948, pt. II.

[2] T. B. A. Senior and J. L. Volakis, *Approximate Boundary Conditions in Electromagnetics*. London, U.K.: IEE Press, 1995.

[3] J. L. Volakis, A. Chatterjee, and L. C. Kempel, *Finite Element Method for Electromagnetics*. New York: IEEE Press, 1998, ch. 2.

[4] K. M. Mitzner, "An integral equation approach to scattering from a body of finite conductivity," *Radio Sci.*, vol. 2, p. 299, 1965.

[5] G. E. Heath, "Impedance boundary condition integral equations," in *Proc. Int. Symp. Antennas Propagat.*, vol. 2, 1984, p. 697.

[6] L. N. Medgyesi-Mitschang and J. M. Putnam, "Integral equation formulations for imperfectly conducting scatters," *IEEE Trans. Antennas Propagat.*, vol. AP-33, pp. 206–214, Feb. 1985.

[7] J. M. Jin, J. L. Volakis, C. L. Yu, and A. C. Woo, "Modeling of resistive sheets in finite element solutions," *IEEE Trans. Antennas Propagat.*, vol. 40, June 1992.

[8] X. C. Yuan, D. R. Lynch, and J. W. Strohbehn, "Three-dimensional finite, boundary, and hybrid element solutions of the Maxwell's equations for lossy dielectric media," *IEEE Trans. Microwave Theory Tech.*, vol. 36, pp. 682–693, Apr. 1988.

[9] Y. Ji and T. H. Hubing, "EMAP5: A 3D hybrid FEM/MoM code," *Appl. Computat. Electromagn. Soc. J.*, vol. 15, no. 1, pp. 1–12, 2000.

[10] A. George and J. W. Liu, *Computer Solution of Large Sparse Positive Definite Systems*. Englewood Cliffs, NJ: Prentice-Hall, 1981.

[11] J. S. Savage and A. F. Peterson, "Higher-order vector finite elements for tetrahedral cells," *IEEE Trans. Microwave Theory Tech.*, vol. 44, pp. 874–879, June 1996.

[12] S. M. Rao, D. R. Wilton, and A. W. Glisson, "Electromagnetic scattering by surfaces of arbitrary shape," *IEEE Trans. Antennas Propagat.*, vol. AP-30, pp. 409–418, May 1982.

[13] J. H. Wang, *Generalized Method of Moments in Electromagnetics*. New York: Wiley, 1990, ch. 7.

[14] Y. Ji, H. Wang, and T. H. Hubing, "A novel preconditioning technique and comparison of three formulations for the hybrid FEM/MoM method," *Appl. Computat. Electromagn. Soc. J.*, vol. 15, pp. 103–114, 2000.

[15] M. W. Ali, T. H. Hubing, and J. L. Drewniak, "A hybrid FEM/MoM technique for electromagnetic scattering and radiation from dielectric objects with attached wires," *IEEE Trans. Electromagn. Compat.*, vol. 39, pp. 304–314, Nov. 1997.

[16] M. G. Andreasen, "Back-scattering cross section of a thin, dielectric, spherical shell," *IRE Trans. Antennas Propagat.*, vol. 5, pp. 267–270, July 1957.

[17] M. Xu, T. H. Hubing, T. P. Van Doren, J. L. Drewniak, and R. E. DuBroff, "Modeling printed circuit boards with embedded decoupling capacitance," in *Proc. 14th Int. Zurich Symp. Electromagnetic Compatibility*, Zurich, Switzerland, Feb. 2001.

[18] C. A. Balanis, *Antenna Theory*, 2nd ed. New York: Wiley, 1997, pp. 454–457.

[19] R. E. Collin, *Field Theory of Guided Waves*. New York: IEEE Press, 1991.

[20] Y. T. Lo, D. Solomon, and W. F. Richards, "Theory and experiment on microstrip antennas," *IEEE Trans. Antennas Propagat.*, vol. AP-27, pp. 137–145, Mar. 1979.

[21] T. Okoshi, *Planar Circuits for Microwaves and Lightwaves*. New York: Springer-Verlag, 1985, ch. 2.

[22] M. Xu, T. H. Hubing, T. P. Van Doren, J. L. Drewniak, and R. E. DuBroff, "Modeling printed circuit boards with embedded decoupling capacitance," in *Proc. 14th Int. Zurich Sympo. Electromagnetic Compatibility*, Zurich, Switzerland, Feb. 2001.

[23] R. Garg, *Microstrip Antenna Design Handbook*. Boston, MA: Artech House, 2001, ch. 1.

[24] H. Wang, Y. Ji, and T. Hubing, "Finite element modeling of coaxial cable feeds and vias in power-bus structures," *IEEE Trans. Electromagn. Compat.*, vol. 44, pp. 569–574, Nov. 2002.

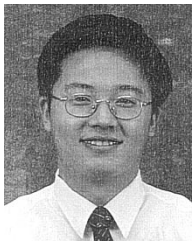

Hao Wang was born in China in 1973. He received the B.S. degree in electrical engineering from Tsinghua University, Beijing, China, in 1996 and the M.S. and Ph.D. degrees in electrical engineering from the University of Missouri-Rolla in 2000 and 2002, respectively.

He is currently applying computer modeling techniques to EMC and signal integrity problems at Micron Technology, Inc., Boise, ID.

Minjia Xu (S'98–M'02) was born in China in 1972. She received the B.S. (with honors) and M.S. degrees in electrical engineering from Tsinghua University, Beijing, China, in 1994 and 1997, respectively, and the Ph.D. degree in electrical engineering from the University of Missouri-Rolla in 2001.

From 1998 to 2001, she was with the Electromagnetic Compatibility Laboratory, University of Missouri-Rolla. She then joined the Hewlett-Packard Company, San Diego, CA, as an EMC engineer in the All-in-One Personal Printing Division. Her current research interests include numerical and experimental analysis of signal integrity and electromagnetic compatibility issues related to printing and faxing products, development of PCB and system-level technology for noise and radiated emission mitigation, as well as design for immunity and electrostatic discharge conformity.

Chen Wang (S'00) received the B.S. and M.S. degrees in electrical engineering, both with honors, from Huazhong University of Science and Technology, Wuhan, China, in 1992 and 1995, respectively. She is currently working toward the Ph.D. degree in ECE at the University of Missouri-Rolla.

From 1995 to 1998, she worked for the Chinese Academcy of Sciences at the Shanghai Institute of Technical Physics, Shanghai, China, designing circuits of infrared sounders on satellites. Her area of specialization has been circuit and system design. Her current research interests include signal integrity and EMI designs in high-speed digital systems, dc power bus, and differential signaling.

Todd Hubing (S'82–M'82–SM'93) received the B.S.E.E. degree from the Massachusetts Institute of Technology, Cambridge, in 1980, the M.S.E.E. degree from Purdue University, West Lafayette, IN, in 1982, and the Ph.D. degree in electrical engineering from North Carolina State University, Raleigh, in 1988.

He is currently a Professor of electrical engineering with the University of Missouri-Rolla (UMR), where he is also a member of the principal faculty in the Electromagnetic Compatibility Laboratory. Prior to joining UMR in 1989, he was an Electromagnetic Compatibility Engineer with IBM, Research Triangle Park, NC. Since joining UMR, the focus of his research has been measuring and modeling sources of electromagnetic interference. He has authored or presented over 100 technical papers, presentations, and reports on electromagnetic modeling and electromagnetic compatibility related subjects.

Dr. Hubing has been a member of the Board of Directors of the IEEE EMC Society since 1995 and is the 2002–2003 President of the Society.